RESEARCH ARTICLE | JUNE 18 2025

Maskless epitaxial overgrowth of diamond on 3D patterns formed by self-organization in an oxidation process

Johannes Fendt ; Matthias Schreck

J. Appl. Phys. 137, 235107 (2025)
https://doi.org/10.1063/5.0269707

Journal of Applied Physics ARTICLE pubs.aip.org/aip/jap

Maskless epitaxial overgrowth of diamond on 3D patterns formed by self-organization in an oxidation process

Cite as: J. Appl. Phys. **137**, 235107 (2025); doi: 10.1063/5.0269707
Submitted: 7 March 2025 · Accepted: 29 May 2025 ·
Published Online: 18 June 2025

View Online Export Citation CrossMark

Johannes Fendt and Matthias Schreck[a)]

AFFILIATIONS

Institut für Physik, Universität Augsburg, Augsburg D-86135, Germany

[a)]**Author to whom correspondence should be addressed:** matthias.schreck@physik.uni-augsburg.de. **Tel.:** +49-821-598-3401.
Fax: +49-821-598-3425.

ABSTRACT

Reduction of the dislocation density (DD) in heteroepitaxial diamond quasi-substrates by maskless epitaxial overgrowth on 3D-patterned surfaces is reported. To create structures appropriate for maskless overgrowth, three different approaches were explored. First, CO_2/H_2 etching in a microwave plasma chemical vapor deposition setup was applied to generate dislocation induced pits. Even for high etch depths of 182 μm, pits with the shape of inverted pyramids aligned along $\langle 110 \rangle$ remained rather small ($\approx 10^{-6}$ cm^2). In the second approach, dry oxidation in a furnace using synthetic air provided structures of suitable size ($>10^{-5}$ cm^2) but insufficient depth. Finally, moisturizing the feed gas reduced the etch velocity by a factor of ≈ 7, but also produced $\langle 100 \rangle$ oriented pits with both high facet angles of $\approx 35°$ and large areas of up to $>10^{-4}$ cm^2. Subsequent maskless overgrowth resulted in a reduction of the initial DD by more than one order of magnitude down to 1.7×10^6 cm^{-2}. Repetition of the etching/overgrowth sequence is expected to facilitate further improvement. The novel technique of self-organized 3D pattern formation is applicable to as-grown surfaces without the need for polishing and lithography. It provides a simple, robust, and scalable concept to improve the structural quality of diamond wafers.

I. INTRODUCTION

Due to its unique material parameters, diamond is considered the ultimate wide bandgap semiconductor material.[1] To harness these beneficial properties, high-quality single-crystal substrates in technologically relevant wafer dimensions are needed. As recently shown, heteroepitaxy on Ir/YSZ/Si with YSZ = yttria stabilized zirconia provides a viable concept to meet at least the size requirements.[2] However, the dislocation density (DD) is still very high (typically $\approx 10^7$ cm^{-2} at a thickness of ≈ 2 mm) even after optimized growth procedures that reduce it from the initial $>10^{10}$ cm^{-2} immediately after nucleation. Consequently, current electronic device development is predominantly performed on homoepitaxial substrates.

The initial DD values of 10^9–10^{10} cm^{-2}, in the early stage of film growth, are not unusual for alternative semiconductor materials grown by heteroepitaxy on foreign substrates with large lattice misfit. Examples are III-nitrides grown on 6H-SiC,[3] Al_2O_3,[4] or Si.[5,6] For their reduction, various variants of the basic concept called epitaxial lateral overgrowth (ELO) have been developed.[7] The most common variant is based on the deposition of a thin layer of a mask material on the semiconductor layer. Then, lithography is applied to form patterns with open window areas in the mask so that the semiconductor crystal can grow homoepitaxially through the window region and expand laterally over the mask. Dislocations below the mask area are stopped, a process occasionally referred to as "filtering". In the window region, they can propagate into the overlayer. The primary factor relevant for the efficiency of this process is the fill factor (FF), given by the ratio between the window area and the total area.[8]

A further parameter that controls the local distribution of dislocations and the reduction of their density in the ELO layer is given by the process conditions. Changing the temperature or gas phase composition typically affects the growth rates in different crystal directions and, as a direct consequence, the faceting of the layer during overgrowth. In the two extreme cases, the threading dislocations from the substrate either continue their perpendicular propagation staying predominantly above the window area or they are tilted away following an inclined facet up to the coalescence region. There, the crystal areas which have grown through neighboring windows meet again to form a closed ELO layer. This variant is called facet-controlled epitaxial lateral overgrowth (FACELO).[9]

Requirements concerning useful mask materials comprise their stability during the overgrowth toward etching or any form of degradation as well as the suppression of any undesired nucleation of the semiconductor material on the mask. In addition, etched mask material should not contaminate the growing crystalline material. All these issues can be avoided completely by maskless ELO. 3D structures are either formed on the hetero-substrate prior to the deposition of the semiconductor layer[6] or via patterning of this layer itself.[10]

In the field of diamonds, ELO-like concepts have been explored by patterning the nucleation layer formed during bias enhanced nucleation (BEN) on iridium.[11] The microneedle method demonstrated by the same research group is a kind of maskless ELO where the gap between the needles is overgrown laterally.[12,13] For the grid patterning approach, a minimum average DD of $9 \times 10^6\,\mathrm{cm}^{-2}$ was reported.[11] Finally, a local reduction of DD by overgrowth over large gaps ($2 \times 2\,\mathrm{mm}^2$, $500 \times 500\,\mu\mathrm{m}^2$),[14,15] also known as aspect ratio trapping (ART), has been demonstrated successfully. Its application for global homogeneous DD reduction on the whole sample surface is still pending.

All concepts described are technologically rather complex. They need flat, typically polished surfaces and lithography steps or laser patterning. In the present work, we explore a new approach for the creation of 3D patterns on dislocation-rich quasi-substrates suitable for overgrowth to obtain an efficient DD reduction. The concept is based on the oxidation of vicinal (001) surfaces. As already reported by various other groups (see summary in Table I), 3D pits can be formed on the (001) surfaces of diamond single crystals by etching using different gas mixtures and activation methods. Under plasma conditions, the etch pits are aligned along ⟨110⟩. Under thermal oxidation, researchers found alignment along ⟨100⟩ at low temperatures and along ⟨110⟩ at high temperatures. The facet tilt angles were predominantly rather small and varied over a wide range from 2° up to several 10°. In addition, the maximum structure size was typically correlated with DD. On type IIa crystals with higher DD, the pits hampered each other's lateral expansion so that they stayed small.[21]

Based on this state of the art, our work was focused on the following basic questions: Is it possible to reproducibly create etch pits with high facet angles greater than 30°? Can one overcome the barrier between neighboring pits to form large structures with areas containing thousands of dislocations? Finally, can these structures be overgrown in a way so that the dislocation density at the surface is reduced significantly? Our work shows that all these challenges can be met yielding at the end unrivaled low dislocation densities for single crystals synthesized by heteroepitaxy. Moreover, the new approach works on as-grown surfaces without the need for polishing.

II. EXPERIMENTAL

Diamond crystals for the present experiments were grown by heteroepitaxy on the multilayer substrate Ir/YSZ/Si(001). Their synthesis comprised the growth of an oxide film by pulsed laser deposition (PLD) on a 4-in. Si(001) wafer with an off-axis tilt angle of 4° toward [110], the deposition of the iridium layer by e-beam evaporation, followed by the nucleation of epitaxial diamond using the bias enhanced nucleation (BEN) procedure in a microwave plasma chemical vapor deposition (MWPCVD) setup.[23,24] In a 915-MHz reactor with a maximum power of 30 kW, 1–2 mm thick diamond layers were then grown using typical gas compositions of 8% CH_4 in H_2 and 20–25 ppm N_2. Afterward, the substrate was removed completely and $5 \times 5\,\mathrm{mm}^2$ crystals were shaped by laser cutting. Their growth surface was either polished mechanically or the samples were utilized as-grown.

In series #1 of the patterning experiments, etching was performed in a 2.45-GHz MWPCVD setup using 10% CO_2 in H_2 at 920 °C. This corresponds to slightly harsher conditions than the standard parameters applied to create etch pits for the quantification of the dislocation density (5% CO_2 in H_2 at 920 °C). Step-by-step, the duration was extended to a maximum time of 30 h in order to monitor the evolution of pit shape and size.

In series #2, a tube furnace with a temperature range up to 1300 °C was used. The diamond samples were placed on a corundum plate inside a 0.5-in. inner diameter quartz tube. A constant flow of dry synthetic air at ambient pressure was maintained during the experiments through the tube using a mass flow controller. For etching with moisturized air in series #3, the feed gas

TABLE I. Literature reports on etch pit formation by oxidation on diamond (001) surfaces using plasma or thermal activation of the gas phase in a furnace.

Reference	Surface/sample	Gas mixture	Activation technique	Temperature (°C)	Pit alignment	Facet tilt angle (°)
Tsubouchi *et al.*[16]	HPHT Ib	1.8% O_2 in H_2	Plasma	850 and 970	⟨110⟩	2–7
Naamoun *et al.*[17]	HPHT type-Ib CVD type-IIa	2% O_2 in H_2	Plasma	830	⟨110⟩	≈25
Ichikawa *et al.*[18]	Ir/MgO CVD	H_2	Plasma	900	⟨110⟩	17–36
Achard *et al.*[19]	HPHT type-Ib	2% O_2 in H_2	Plasma	830	⟨110⟩	≈25
Evans and Sauter[20]	Natural	air	Thermal	775 and 1400	⟨100⟩ at 775 °C ⟨110⟩ at 1400 °C	…
de Theije *et al.*[21]	Type-Ia, -Ib, and -IIa	10% O_2 in Ar dry	Thermal	700–900	<100> for <750° C, <110> for >750° C	2–15
de Theije *et al.*[22]	Type-Ia, -Ib, and -IIa	10% O_2 in Ar moisturized	Thermal	700–900	⟨110⟩	5–11

was passed through a bubbler containing demineralized water. The furnace was heated up at a position 40 cm downstream from the location where the sample was placed inside the quartz tube. After having reached the preset temperature value, the furnace was shifted to the sample position and later back, in order to achieve a steep temperature ramp with rapid start and termination of the etching, respectively.

Overgrowth of the patterned samples was done in the 2.45-GHz MWPCVD setup using the parameters shown later.

The removal rate was derived from thickness measurements with a high precision caliper. In addition, the weight loss was determined. To measure the topography of the etched surface quantitatively, a confocal 3D laser scanning microscope (LSM) (Keyence VK-X1000) equipped with a 404 nm laser was used. Its accuracy and high dynamic range were ideally suited for the present experiments and facilitated accurate measurements of feature size, depth, and tilt angles of the facets. Scanning electron microscopy (SEM) was applied to obtain high resolution images of specific surface features.

III. RESULTS

The typical DD values of heteroepitaxial diamond quasi-substrates with a thickness of 1–2 mm are on the order of $2–10 \times 10^7\ \mathrm{cm}^{-2}$.[25] This corresponds numerically to an area of $1–5 \times 10^{-8}\ \mathrm{cm}^2$ per dislocation. In order to achieve appreciable reduction effects by overgrowth, we aimed at structures with 2–3 orders of magnitude larger areas, i.e., $>10^{-5}\ \mathrm{cm}^2$ equivalent to lateral dimensions $>30\ \mu$m. This was the guideline for the experiments described in the following.

A. Plasma etching in the MWPCVD setup

Figures 1(a)–1(d) show the evolution of the etch patterns formed in a MWPCVD reactor with process time on a 1.4 mm thick heteroepitaxial quasi-substrate. After 25 min [see Fig. 1(a)], the surface is covered by individual pits that facilitate the derivation of the dislocation density. After 5 h and removal of 35 μm, the whole surface is densely covered with etch pits without space in between. Their basic shape of inverted pyramids with the edges aligned along ⟨110⟩ is preserved but their density has decreased by a factor of five. Slight asymmetries are attributed to the off-axis angle of the surface. In further treatments of this sample, for 5 additional hours in the third and 20 additional hours in the fourth step, the further decrease in pit density is only by a factor of two. The entire reduction in pit density from 2.2×10^7 to $2.4 \times 10^6\ \mathrm{cm}^{-2}$ corresponds to one order of magnitude. However, the large

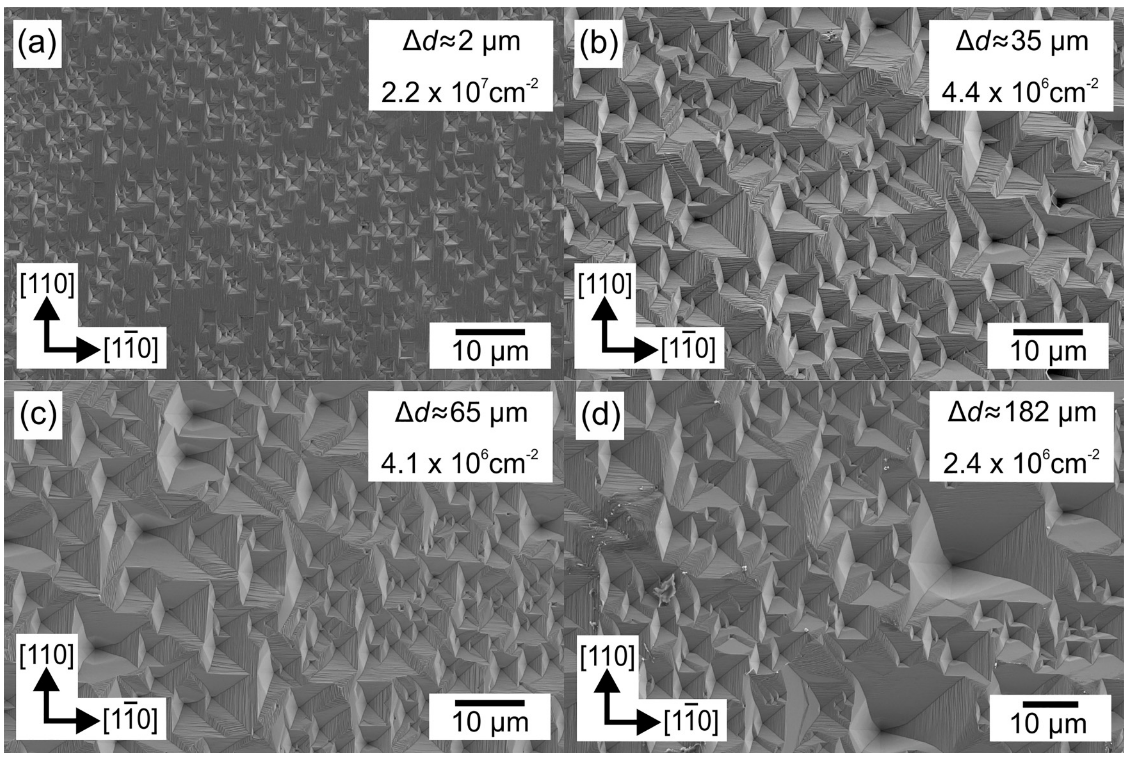

FIG. 1. SEM images of etch pits formed in a MWPCVD reactor at 920 °C using a gas mixture of 10% CO_2/H_2 at a gas pressure of 160 mbar. Sample orientation: step flow direction is [1$\bar{1}$0], i.e., the [001] crystal axis is tilted leftward. Total exposure time: (a) 25 min, (b) 25 min + 4 h 35 min, (c) 5 + 5 h, and (d) 5 + 5 + 20 h. Δd corresponds to the accumulated material removal. Average etch rate: ≈6 μm/h. Average tilt angle of the facets measured along [110] is 33 ± 4° close to the value for (112) crystal planes.

majority of etch pits remained small (<10 μm) even after the total removal of 182 μm. Since the average pit area of $\approx 9 \times 10^{-7}$ cm^2 is still well below the target value of $>10^{-5}$ cm^2, plasma etching under the present conditions can apparently not provide a route to surface structures large enough for maskless overgrowth.

B. Etching by synthetic air in a tube furnace

Alternative patterning strategies were explored by oxidation at ambient pressure in a tube furnace using synthetic air. The experiments were performed in the temperature range from 715 to 895 °C for dry and between 675 and 995 °C for moisturized air. The variations of the oxidation velocities with temperature are plotted in Fig. 2.

The etch rates in Fig. 2 vary between ≈1 and more than 1000 μm/h. The most prominent difference between the red and black data points is a reduction of the etch rate by roughly a factor of 7–8 when the synthetic air is moisturized.

Linear fits in the Arrhenius plots yield similar activation energies of $E_{A,dry} = 224 \pm 12$ kJ mol^{-1} and $E_{A,moisturized} = 217 \pm 4$ kJ mol^{-1} for etching in dry and moisturized air, respectively. The main difference is the pre-exponential factor in the Arrhenius equation. Activation energies are higher than literature data obtained for the oxidation of (001) single crystal surfaces, such as 199 kJ mol^{-1} (atmospheric pressure oxidation in pure O_2 of natural crystals)[26] or 186 kJ mol^{-1} (atmospheric pressure oxidation with 10% O_2 in Ar).[21] They are close to the value of 229 kJ mol^{-1} reported for polycrystalline CVD films.[26]

In all experiments, oxidation on the (001) surface resulted in pit formation and a pronounced roughening which excludes again a simple layer-by-layer removal mechanism. Instead, it proves a defect-controlled process. To assess the topography in terms of the intended application for maskless 3D overgrowth, shape and size of the created structures were analyzed by SEM and LSM (see Fig. 3).

The SEM image displayed in Fig. 3(a) shows a surface consisting of large pits in the shape of inverted pyramids with fourfold symmetry. Their sizes range between 10^{-6} and 10^{-4} cm^2. Their facets aligned along [100] and [010] are dominated by macrosteps. Figure 3(b) shows a magnified LSM image of the same spot, and in (c) and (d), the derived height profiles taken along two perpendicular directions. In both cases, the angles of the facets on the right side are significantly higher than on the left side. Statistical data acquired for 33 etch pits yield a bimodal distribution [Fig. 3(e)]. The average inclination angles of opposing facets are 13.1° and 18.6° equivalent to a difference of 5.5°. This asymmetry in the [100] direction and also in the [010] direction nicely agrees with the values calculated for an average facet angle of 15.8° relative to the crystallographic [001] axis on a surface with a global off-axis tilt angle of 4.5°. The tilt angle of the (001) surface can be removed numerically in the LSM height data set so that the crystallographic [001] axis is exactly perpendicular. Then, a monomodal distribution is obtained as shown in Fig. 3(f). This result proves that all four facets correspond to the identical family of high index crystal planes ((027), $(0\bar{2}7)$, (207), $(\bar{2}07)$). While the size of the pits is in an appropriate range, the average angle of 15.8° is rather low compared to the typical aspect ratio of maskless ELO structures used for other semiconductor layers as reported in the literature.

In a further experimental series, the synthetic air was moisturized before it was fed into the quartz tube.

The SEM images of the sample series in Figs. 4(a)–4(d) show rather steep etch pits with smooth facets aligned along [100] and [010]. Their area density decreased from 6.4×10^6 to 3.2×10^3 cm^{-2} accompanied by a corresponding size increase for the individual pits.

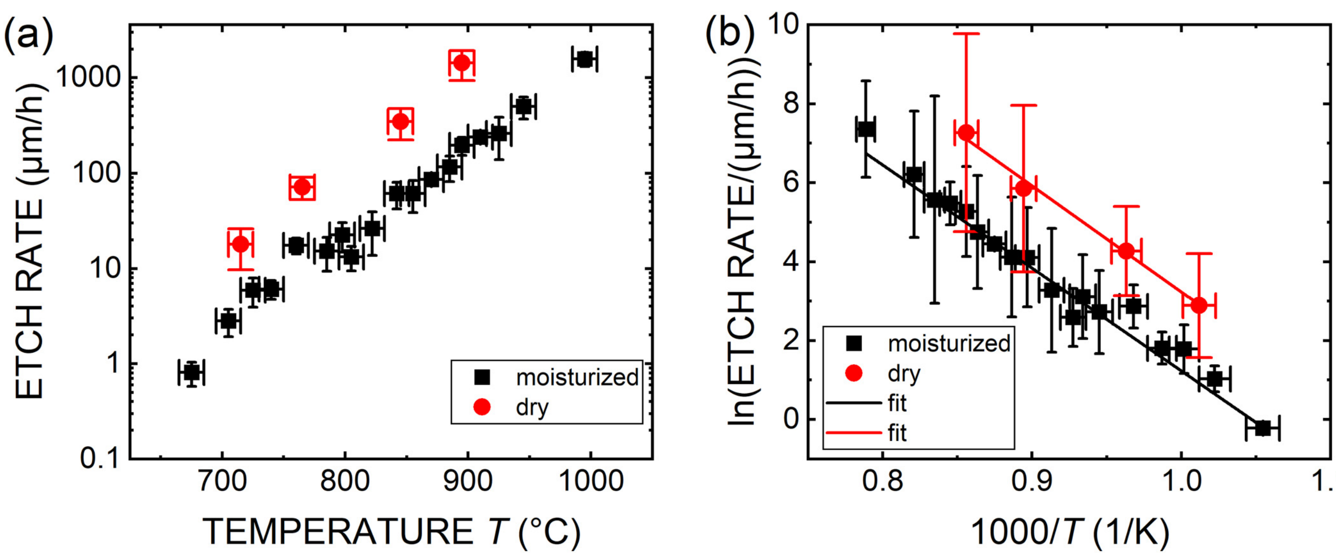

FIG. 2. (a) Etch rate vs temperature and (b) the corresponding Arrhenius-plot for oxidation at ambient pressure in moisturized and dry synthetic air, respectively. Material removal was measured on the (001) surface corresponding to the former growth surface.

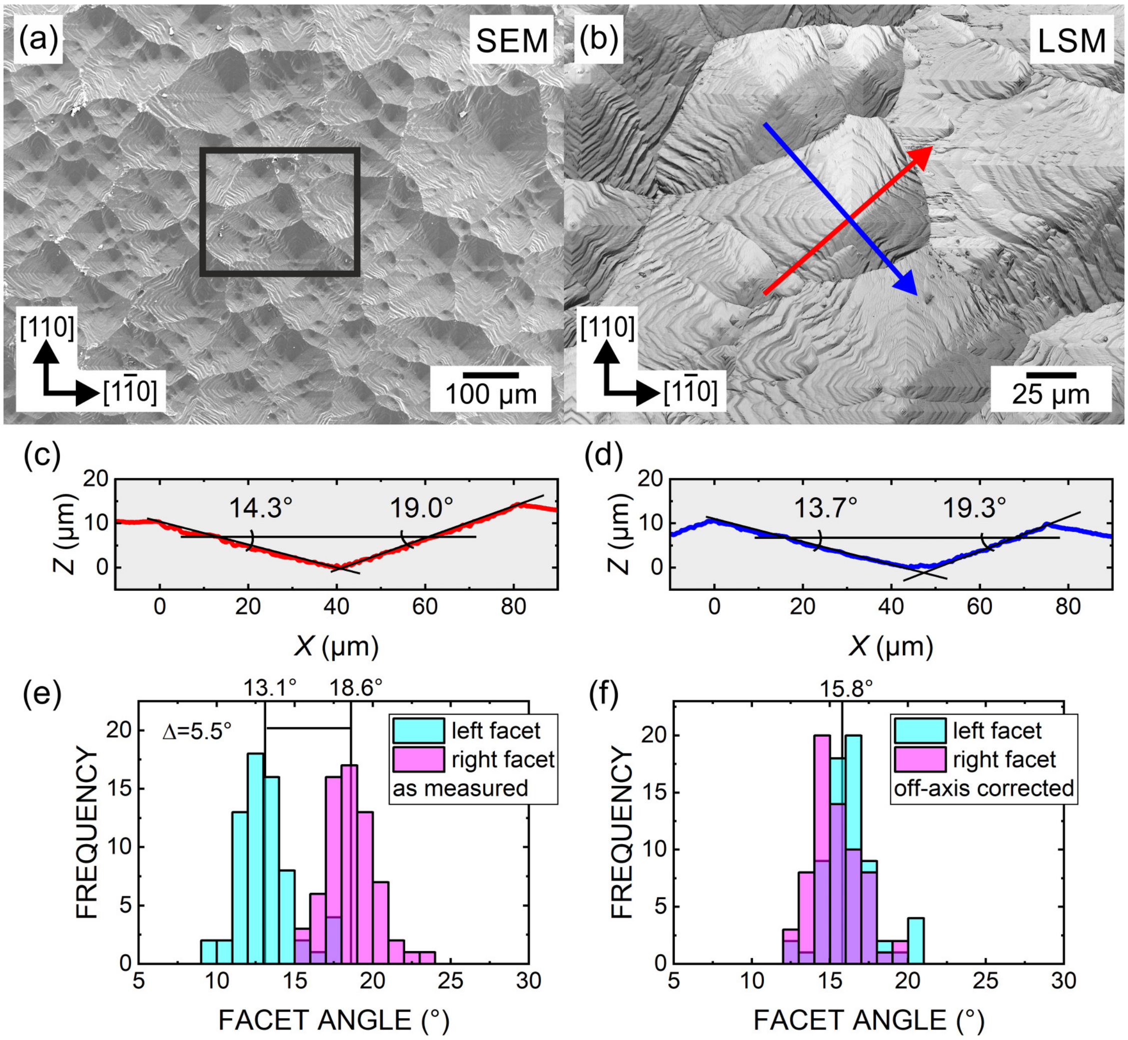

FIG. 3. (a) SEM images of a diamond sample oxidized in dry synthetic air for 1 h at 845 °C. Step flow direction is [1$\bar{1}$0], i.e., the [001] crystal axis is tilted leftward. The material removal amounts to 280 μm. (b) Magnified LSM image of the identical spot. (c) and (d) Surface profiles taken along the red and blue lines in (b). (e) Histogram of the facet angles measured along the [100] or [010] direction, respectively. (f) Histogram after numerical removal of the off-axis tilt.

Figure 5 shows the zoomed LSM intensity image of an individual pit with an area of 2.3×10^{-5} cm^2. It was formed at 845 °C by the removal of 110 μm. According to the line scans derived from the LSM height map, its depth is 16 μm and the side facets have roughly identical inclination angles with an average value of ≈35°. This is in clear contrast to the observation in Fig. 3 where the as-measured values differed by 5.5° and became identical after numerical removal of the off-axis angle proving that the facet angles were crystallographically identical. Here, the angles relative to the physical surface are roughly identical, meaning that opposing facets correspond to different crystal planes.

Statistically, ≈10^3 dislocations are located inside the area of the present pit. They end on the side faces of the inverted pyramid. Nevertheless, these facets are extremely smooth without any indication of local etching structures due to dislocations emerging at the surface. Of high relevance and quite beneficial for the later overgrowth is also the observation that neighboring pits are often separated by rather narrow ridges [see Fig. 5(c)].

The increase in the average pit area and the concomitant decrease in the pit density were evaluated systematically for a greater number of samples with the etch depth ranging from few micrometers up to 510 μm. The results are displayed in Fig. 6.

The data in Fig. 6 demonstrate the pronounced decrease in the pit density from the initial ≈10^7 to below 10^4 cm^{-2}. Concomitantly, the average pit area increased from ≈10^{-7} to >10^{-4} cm^2. For the samples with an etch depth >200 μm, statistically several thousand

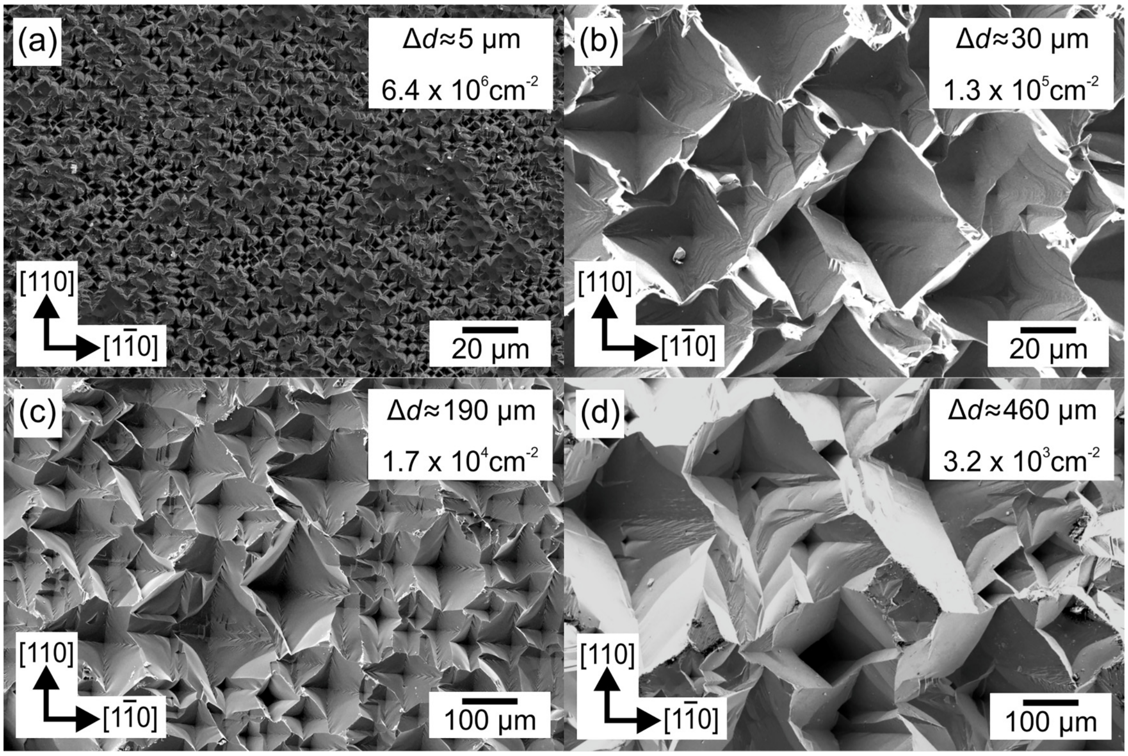

FIG. 4. (a)–(d) SEM images of the diamond samples etched at 845 °C for 5 min, 25 min, 2.5 h, and 5 h in a flow of moisturized synthetic air. Step flow direction is [1$\bar{1}$0], i.e., the [001] crystal axis is tilted leftward.

dislocations are located inside each hole. Appropriate process conditions should facilitate burying most of these defects by lateral overgrowth so that they end inside the crystal resulting in a reduced dislocation density at the growth surface.

C. Maskless 3D overgrowth experiments

Several quasi-substrates patterned by oxidation in moisturized air at 840° for 5 h were overgrown in a MWPCVD setup using the parameters listed in Table II. SEM images of one specific sample before patterning and after overgrowth are shown in Fig. 7.

The surface after overgrowth is rather flat with some step bunching as typical for off-axis grown samples of this thickness. Deep holes resulting from incomplete coalescence are absent. Steep steps as visible in the intermediate stages for a sample processed under identical conditions (see Appendix A) have been smoothened by the step flow growth mode on the off-axis substrate. This process has also redistributed the dislocations so that coalescence boundaries are no longer visible. The comparison of (b) and (c) illustrates the scatter in the local DD. Quantitative evaluation of the DD is presented in Fig. 8.

The data in Fig. 8 show a substantial reduction in the dislocation density from $\approx 5 \times 10^7$ to $1.7(\pm 0.9) \times 10^6\ \mathrm{cm}^{-2}$ by the oxidation in moisturized air and the subsequent maskless 3D overgrowth. Extrapolating the $1/d$ curve to higher thicknesses, a comparable reduction by simple growth would require a final thickness of ≈30 mm.

IV. DISCUSSION AND SUMMARY

In this study, three different concepts have been explored to create three-dimensional patterns with size and shape appropriate for subsequent maskless 3D overgrowth to reduce the DD. Common to all is the back etching of dislocation-rich substrates accompanied by the emergence of etch patterns in a self-organized way without the need for elaborate deterministic steps like the preparation of ELO masks by photolithography. Table III summarizes the crucial results.

The etching in the MWPCVD reactor using a CO_2/H_2 gas mixture yielded high initial densities of pits with steep faces of 33°. With progressing etch depth, their density decreased, while the size increased by roughly one order of magnitude. However, even after the removal of $182\,\mu$m, the lateral dimensions of the individual structures were still insufficient in size. In series #2, the oxidation in a tube furnace by dry synthetic air provided large pits. In this case, with facet angles of ≈16°, the aspect ratio of the structures was too low. Oxidation in moisturized air as the third method finally provided both: pits with individual areas in the range of $10^{-4}\ \mathrm{cm}^2$ and steep facet angles of ≈35°. Moisturized air slowed down the etching rate by a factor of 7–8.

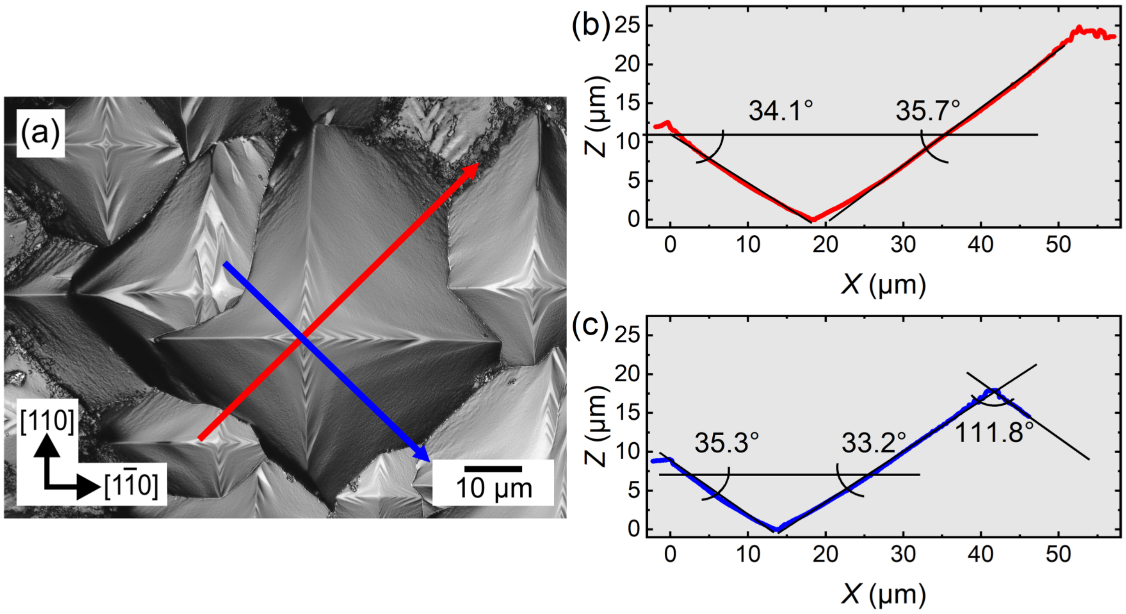

FIG. 5. (a) Magnified LSM intensity image of an etch pit obtained after the removal of 110 μm at 845 °C. (b) and (c) Line profiles derived from LSM height data along the red and blue lines, respectively. Step flow direction is [1$\bar{1}$0], i.e., the [001] crystal axis is tilted leftward.

For the explanation of all these observations, the role of the dislocations will be considered first. In their core (diameter <1 nm), the crystal lattice is heavily distorted which results in a reduced bonding strength for the carbon atoms. Etchants will preferentially attack the diamond crystal at this position. Facet formation around this weak point is then an issue of anisotropic etching. It is a common phenomenon known from the etching of different types of single crystals that the etching velocities in different crystal directions vary with process temperature, etchant composition, as well as the activation method.[28,29] This can substantiate, in a very general way, the 45°-rotation of the pits between our plasma and furnace experiments. de Theije *et al.*[21,22] identified in

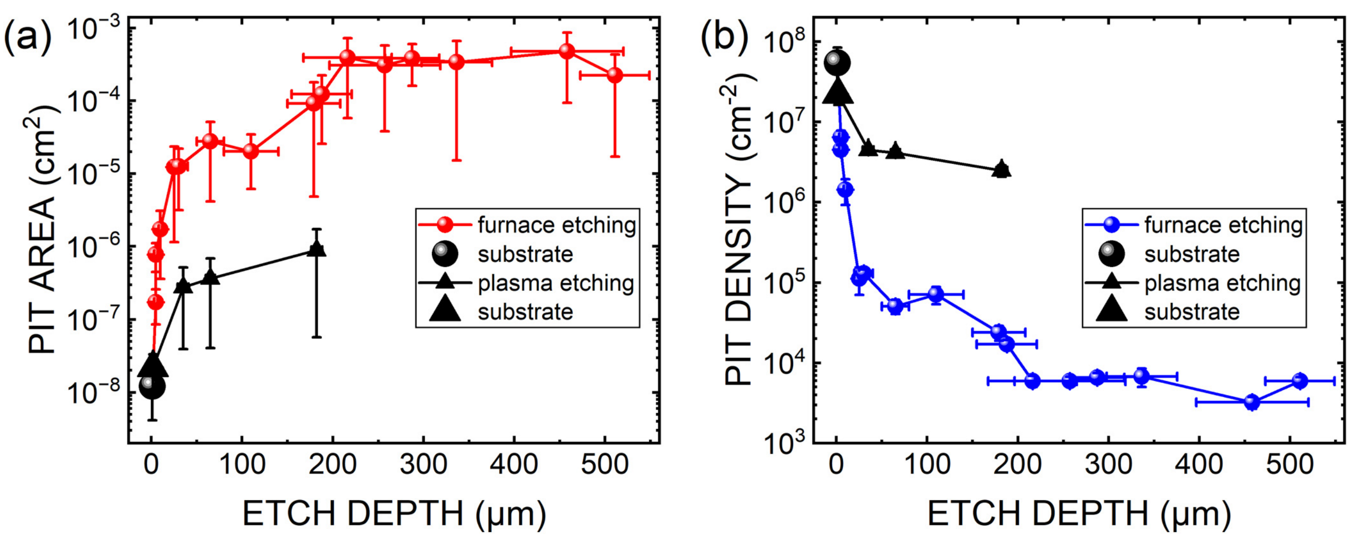

FIG. 6. (a) Average area and (b) density of etch pits vs etch depth derived for a series of samples after oxidation in moisturized synthetic air at 845 °C. For direct comparison, the results obtained by plasma etching using 10% CO_2/H_2 in the MWPCVD setup (see Fig. 1) are included as black data points.

TABLE II. Process conditions for the three-step 3D overgrowth process.

Step	Duration (h)	Temperature (°C)	CH_4/H_2 (%)	N_2 (ppm)	Pressure (mbar)
1	5	1000	4	25	150
2	5	1000	4	25	150
3	20	1000	8	25	150

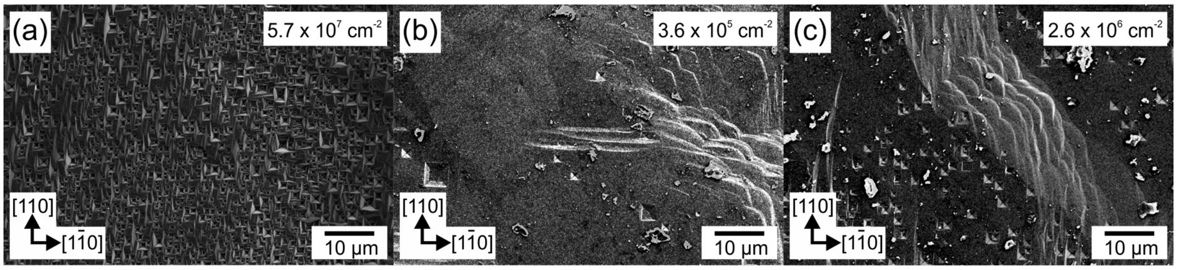

FIG. 7. SEM micrographs of the etch pit distributions for (a) the as-grown surface of the quasi-substrate before patterning, (b) and (c) as-grown surface of the same substrate after furnace oxidation in moisturized air and three consecutive maskless overgrowth steps. The average value of the etch pit density after the final overgrowth step is $1.7(\pm 0.9) \times 10^6$ cm^{-2}. Step flow direction is [1$\bar{1}$0], i.e., the [001] crystal axis is tilted leftward.

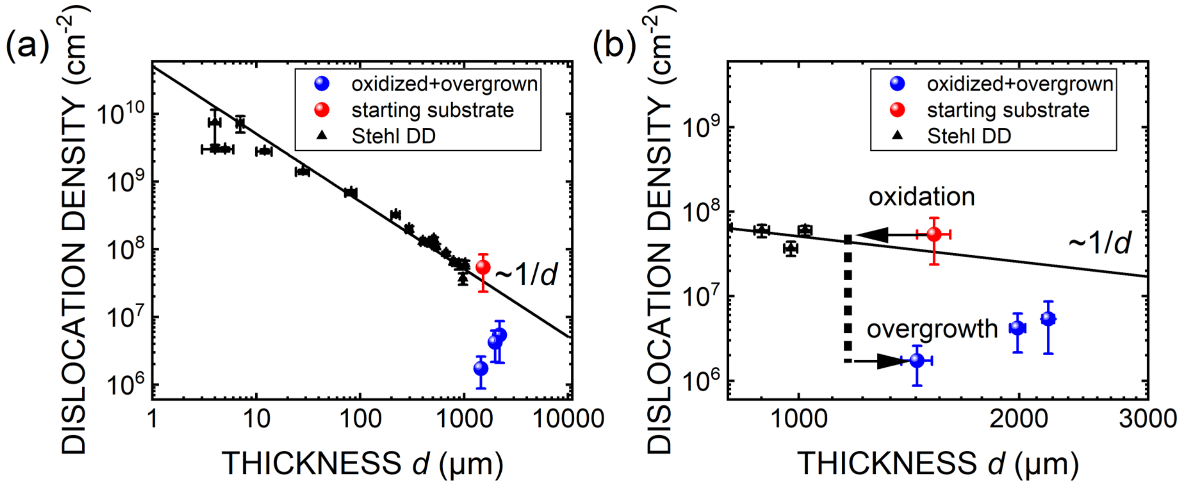

FIG. 8. (a) Reduction of the DD by maskless 3D overgrowth in direct comparison to the literature reports on the 1/*d* behavior (black triangles and straight line from Stehl *et al.*[27]). Red data point: starting substrate with DD $\approx 5 \times 10^7$ cm^{-2}. Its initial thickness of 1.53 mm was first reduced to 1.19 mm by oxidation in moisturized air and then increased to 1.45 mm by the 3D overgrowth processes (left blue sphere). Two further blue spheres show results from additional processes using pieces of the same wafer. Error bars indicate the local variation in DD. (b) Zoom into the relevant thickness region.

TABLE III. Conditions and experimental results obtained in the three etching series. For the derivation of the tilt angles, the left-hand and right-hand values were averaged for each pit.

No.	Activation technique	Gas mixture	Temperature (°C)	Pit alignment	Facet tilt angle (average)	Maximum average pit area
1	Plasma	10% CO_2 in H_2	920	$\langle 110 \rangle$	$33 \pm 4°$	9×10^{-7} cm^2 at 182 μm
2	Thermal	Dry air	845	$\langle 100 \rangle$	$15.8 \pm 3.2°$	7×10^{-5} cm^2 at 280 μm
3	Thermal	Moisturized air	845	$\langle 100 \rangle$	≈35° (at 110 μm etch depth)	3–5 $\times 10^{-4}$ cm^2 above 200 μm

their thermal oxidation experiments the temperature as the crucial parameter which changed the alignment along ⟨100⟩ at temperatures below ≈750 °C to ⟨110⟩ at high temperatures for dry etching. In moisturized air, they found no rotation.

Under equilibrium conditions, the formation of facets equivalent to low index crystal lattice planes is expected. However, the huge variation of the tilt angles in Table I already indicates that the facet shape is predominantly controlled by the kinetics of the etching processes rather than thermodynamic equilibrium. The reduction in the etch rate by a factor 7–8 on moisturization of the synthetic air as well as the change from the rough facets with a low average crystallographic tilt angle of 15.8° (dry, see Fig. 3) to steep smooth facets (moisturized, see Figs. 4 and 5) provide further insight into the relevant mechanisms. The dangling bonds of the covalent diamond surface are saturated by different species (O, H, and OH) when water is added to the synthetic air. The resulting smooth surface is typically interpreted in terms of step flow processes. While oxygen molecules can attack the diamond lattice easily all over the facet area under dry conditions resulting in a rough surface, in moisturized air, the removal proceeds preferentially at the kink position of step edges and is, therefore, drastically slowed down. This can nicely explain that the energy barrier for carbon etching is nearly the same (see activation energies in Fig. 2) but the pre-exponential factor is reduced significantly.

The layer-by-layer removal starts at the location of the dislocation which represents the fastest etching position. Every modification in the process conditions can potentially modify the etching kinetics with the most radical change occurring when the zone axis of the facet planes switches from ⟨100⟩ to ⟨110⟩.

The authors of Ref. 21 had observed a mutual hampering in size increase for neighboring etch pits. In all the present experiments, we found that this barrier is at least partially overcome so that the pit density decreased, and the size of the individual pits increased. However, only the experiments in the furnace showed sufficient dynamic yielding growth of the pit area by more than a factor of 10^3. As shown in Fig. 5, the facets of the pits created in series #3 are very smooth. Since dislocations cannot disappear during the etching process, many dislocations (≈10^3) terminate all over the facet area. Its steep angle apparently prevents them from forming their own individual pit structure so that further evolution of this large pit is exclusively controlled by the dislocation at the apex.

The detailed mechanism of the pit coarsening process is still to be clarified. Considering the two alternative options of (a) neighboring structures merging as equal constituents of the finally emerging pit or (b) the dissolution of one pit inside the other one, the first version can already be rejected. The observation that even pits grown by a factor of 10^3 end at the bottom in one very sharp apex provides clear proof that it is only one specific dislocation ending at this point that controls the shape and evolution of the whole structure. Pit coarsening works via an evolutionary selection mechanism quite similar to Ostwald ripening in the growth of liquid or solid particles.[30]

As a further relevant parameter, the role of the Burgers vector must be considered. Tallaire *et al.*[31] and Ichikawa *et al.*[18] have consistently reported that pits created at edge dislocations are shallower than those formed at 45° mixed type dislocations. Appendix B shows two snapshots taken in one specific surface region in the early stage of etching in series #3 (after 30 and 60 min). The preliminary analysis of the angles reveals that two groups of etch pits can be distinguished. In the competition between shallow slow-etching and steep fast-etching pits, the steep ones seem to win and dominate the structure formation. This suggests that at the apex of large pits, one should predominately find 45° mixed type dislocations. Proving this hypothesis in the future will require delicate lamella preparation inside the deep structures for subsequent Burgers vector analysis by transmission electron microscopy (TEM).

In summary, we have found in this study, oxidation procedures that can generate large size 3D structures with high aspect ratios on diamond (001) surfaces that are useful for maskless 3D overgrowth. The most efficient overgrowth processes tested in this work yielded a reduction of the dislocation density by more than one order of magnitude. A minimum value of $1.7(\pm 0.9) \times 10^6\ \mathrm{cm}^{-2}$ was obtained. Further improvement in the DD is expected by repetition of the patterning and overgrowth procedures. Due to its technological simplicity, robustness, and scalability, we see a great potential of the present approach for the realization of diamond wafers with high structural quality.

ACKNOWLEDGMENTS

We gratefully acknowledge the financial support by the German Research Foundation DFG (Project No. 453637298).

AUTHOR DECLARATIONS

Conflict of Interest

The authors have no conflicts to disclose.

Author Contributions

Johannes Fendt: Formal analysis (lead); Investigation (lead); Validation (equal); Visualization (lead); Writing – original draft (supporting); Writing – review & editing (equal). **Matthias Schreck:** Conceptualization (lead); Data curation (equal); Formal analysis (supporting); Funding acquisition (lead); Investigation (supporting); Methodology (equal); Project administration (lead); Writing – original draft (lead); Writing – review & editing (equal).

DATA AVAILABILITY

The data that support the findings of this study are available from the corresponding author upon request.

APPENDIX A: EVOLUTION OF THE TOPOGRAPHY DURING OVERGROWTH

Imaging the intermediate steps of the overgrowth process facilitates monitoring the progressing filling of the deep etch structures until a closed surface is formed [as displayed before in Figs. 7(b) and 7(c)]. The LSM images in Figs. 9(b)–9(d) show that the narrow ridges created by oxidation are transformed into plateaus that expand continuously. Preparation of cross-sectional samples for a careful study of local dislocation bending and burying is under way.

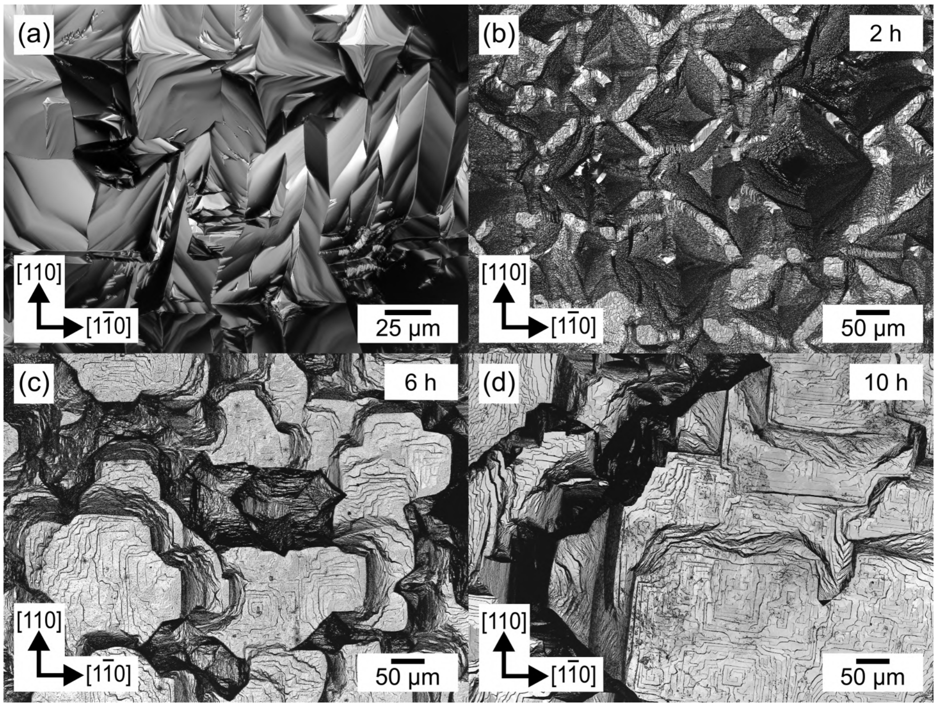

FIG. 9. LSM intensity images of a diamond surface (a) after oxidation and at different stages of the overgrowth process after (b) 2, (c) 6, and (d) 10 h. All images were taken from the same quasi-substrate at different spots of the surface.

APPENDIX B: SNAPSHOTS OF THE SURFACE EVOLUTION

Two snapshots illustrating the surface evolution during the etching in series #3 are shown in Fig. 10. Comparison between (a) and (b) reveals that shallow slower etching pits have been displaced by steeper ones.

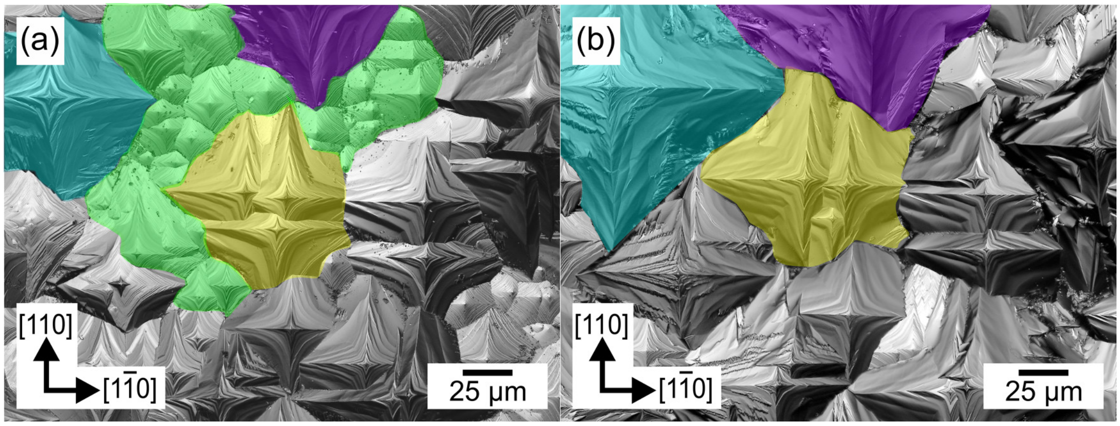

FIG. 10. LSM intensity images of pits generated at 845 °C in moisturized air after (a) 30 and (b) 60 min. The cumulative etch depth is 25 and 65 μm, respectively. As derived from the corresponding height data, the large cyan, yellow, and purple structures have higher average tilt angles (33.3 ± 1.5°) than the small green pits (21.5 ± 2.8°).

REFERENCES

[1] *Power Electronics Device Applications of Diamond Semiconductors*, edited by S. Koizumi, H. Umezawa, J. Pernot, and M. Suzuki (Elsevier Ltd., 2018).

[2] M. Schreck, S. Gsell, R. Brescia, and M. Fischer, "Ion bombardment induced buried lateral growth: The key mechanism for the synthesis of single crystal diamond wafers," Sci. Rep. **7**, 44462 (2017).

[3] F. R. Chien, X. J. Ning, S. Stemmer, P. Pirouz, M. D. Bremser, and R. F. Davis, "Growth defects in GaN films on 6H-SiC substrates," Appl. Phys. Lett. **68**, 2678 (1996).

[4] X. J. Ning, F. R. Chien, P. Pirouz, J. W. Yang, and M. Asif Khan, "Growth defects in GaN films on sapphire: The probable origin of threading dislocations," J. Mater. Res. **11**, 580 (1996).

[5] P. Saengkaew, A. Dadgar, J. Blaesing, T. Hempel, P. Veit, J. Christen, and A. Krost, "Low-temperature/high-temperature AlN superlattice buffer layers for high-quality $Al_xGa_{1-x}N$ on Si (111)," J. Cryst. Growth **311**, 3742 (2009).

[6] A. Strittmatter, S. Rodt, L. Reißmann, D. Bimberg, H. Schröder, E. Obermeier, T. Riemann, J. Christen, and A. Krost, "Maskless epitaxial lateral overgrowth of GaN layers on structured Si(111) substrates," Appl. Phys. Lett. **78**, 727 (2001).

[7] K. Hiramatsu, "Epitaxial lateral overgrowth techniques used in group III nitride epitaxy," J. Phys.: Condens. Matter **13**, 6961 (2001).

[8] P. Fini, H. Marchand, J. P. Ibbetson, S. P. DenBaars, U. K. Mishra, and J. S. Speck, "Determination of tilt in the lateral epitaxial overgrowth of GaN using x-ray diffraction," J. Cryst. Growth **209**, 581 (2000).

[9] K. Hiramatsu, K. Nishiyama, M. Onishi, H. Mizutani, M. Narukawa, A. Motogaito, H. Miyake, Y. Iyechika, and T. Maeda, "Fabrication and characterization of low defect density GaN using facet-controlled epitaxial lateral overgrowth (FACELO)," J. Cryst. Growth **221**, 316 (2000).

[10] T. M. Katona, P. Cantu, S. Keller, Y. Wu, J. S. Speck, and S. P. DenBaars, "Maskless lateral epitaxial overgrowth of high-aluminum content $Al_xGa_{1-x}N$," Appl. Phys. Lett. **84**, 5025 (2004).

[11] K. Ichikawa, K. Kurone, H. Kodama, K. Suzuki, and A. Sawabe, "High crystalline quality heteroepitaxial diamond using grid-patterned nucleation and growth on Ir," Diamond Relat. Mater. **94**, 92 (2019).

[12] H. Aida, S.-W. Kim, K. Ikejiri, D. Fujii, Y. Kawamata, K. Koyama, H. Kodama, and A. Sawabe, "Microneedle growth method as an innovative approach for growing freestanding single crystal diamond substrate: Detailed study on the growth scheme of continuous diamond layers on diamond microneedles," Diamond Relat. Mater. **75**, 34 (2017).

[13] H. Aida, S.-W. Kim, K. Ikejiri, Y. Kawamata, K. Koyama, H. Kodama, and A. Sawabe, "Fabrication of freestanding heteroepitaxial diamond substrate via micropatterns and microneedles," Appl. Phys. Express **9**, 035504 (2016).

[14] A. Tallaire, O. Brinza, V. Mille, L. William, and J. Achard, "Reduction of dislocations in single crystal diamond by lateral growth over a macroscopic hole," Adv. Mater. **29**, 1604823 (2017).

[15] L. Mehmel, R. Issaoui, O. Brinza, A. Tallaire, V. Mille, J. Delchevalrie, S. Saada, J. C. Arnault, F. Bénédic, and J. Achard, "Dislocation density reduction using overgrowth on hole arrays made in heteroepitaxial diamond substrates," Appl. Phys. Lett. **118**, 061901 (2021).

[16] N. Tsubouchi, Y. Mokuno, and S. Shikata, "Characterizations of etch pits formed on single crystal diamond surface using oxygen/hydrogen plasma surface treatment," Diamond Relat. Mater. **63**, 43 (2016).

[17] M. Naamoun, A. Tallaire, F. Silva, J. Achard, P. Doppelt, and A. Gicquel, "Etch-pit formation mechanism induced on HPHT and CVD diamond single crystals by H_2/O_2 plasma etching treatment," Phys. Status Solidi A **209**, 1715 (2012).

[18] K. Ichikawa, H. Kodama, K. Suzuki, and A. Sawabe, "Dislocation in heteroepitaxial diamond visualized by hydrogen plasma etching," Thin Solid Films **600**, 142 (2016).

[19] J. Achard, F. Silva, O. Brinza, X. Bonnin, V. Mille, R. Issaoui, M. Kasu, and A. Gicquel, "Identification of etch-pit crystallographic faces induced on diamond surface by H_2/O_2 etching plasma treatment," Phys. Status Solidi A **206**, 1949 (2009).

[20] T. Evans and D. H. Sauter, "Etching of diamond surfaces with gases," Philos. Mag. **6**, 429 (1961).

[21] F. K. de Theije, N. J. van der Laag, M. Plomp, and W. J. P. van Enckevort, "A surface topographic investigation of {001} diamond surfaces etched in oxygen," Philos. Mag. A **80**, 725 (2000).

[22] F. K. de Theije, O. Roy, N. J. van der Laag, and W. J. P. van Enckevort, "Oxidative etching of diamond," Diamond Relat. Mater. **9**, 929 (2000).

[23] S. Gsell, T. Bauer, J. Goldfuß, M. Schreck, and B. Stritzker, "A route to diamond wafers by epitaxial deposition on silicon via iridium/yttria-stabilized zirconia buffer layers," Appl. Phys. Lett. **84**, 4541 (2004).

[24] S. Gsell, M. Fischer, T. Bauer, M. Schreck, and B. Stritzker, "Yttria-stabilized zirconia films of different composition as buffer layers for the deposition of epitaxial diamond/Ir layers on Si(001)," Diamond Relat. Mater. **15**, 479 (2006).

[25] M. Schreck, P. Ščajev, M. Träger, M. Mayr, T. Grünwald, M. Fischer, and S. Gsell, "Charge carrier trapping by dislocations in single crystal diamond," J. Appl. Phys. **127**, 125102 (2020).

[26] Q. Sun and M. Alam, "Relative oxidation behavior of chemical vapor deposited and type IIa natural diamonds," J. Electrochem. Soc. **139**, 933 (1992).

[27] C. Stehl, M. Fischer, S. Gsell, E. Berdermann, M. S. Rahman, M. Traeger, O. Klein, and M. Schreck, "Efficiency of dislocation density reduction during heteroepitaxial growth of diamond for detector applications," Appl. Phys. Lett. **103**, 151905 (2013).

[28] P. Pal and K. Sato, "A comprehensive review on convex and concave corners in silicon bulk micromachining based on anisotropic wet chemical etching," Micro Nano Syst. Lett. **3**, 6 (2015).

[29] D. Zhuang and J. H. Edgar, "Wet etching of AgN, AlN, and SiC: A review," Mater. Sci. Eng. R **48**, 1 (2005).

[30] M. Kahlweit, "Ostwald ripening of precipitates," Adv. Colloid Interface Sci. **5**, 1 (1975).

[31] A. Tallaire, T. Quisse, A. Lantreibecq, R. Cours, M. Legros, H. Bensalah, J. Barjon, V. Mille, O. Brinza, and J. Achard, "Identification of dislocations in synthetic chemically vapor deposited diamond single crystals," Cryst. Growth Des. **5**, 2741 (2016).